RSC Advances

ROYAL SOCIETY OF CHEMISTRY

PAPER

View Article Online
View Journal | View Issue

Cite this: *RSC Adv.*, 2025, **15**, 435

High red luminescence intensity under sunlight exposure of a PMMA polymer doped with a tetrakis Eu^{3+} β-diketonate complex containing a benzimidazolium counterion†

Israel P. Assunção, *[a,b] Israel F. Costa, [a] Lucca Blois, [a] Maria Claudia F. C. Felinto,[c] Victor M. Deflon,[d] Rômulo A. Ando, [a] Oscar L. Malta[e] and Hermi F. Brito*[a]

New tetrakis Eu^{3+} and Gd^{3+} β-diketonate complexes containing benzimidazolium (Bzim) as the counterion were synthesized by the one-pot method. The Bzim[Eu(tta)$_4$]·H$_2$O complex was further incorporated into a poly(methyl methacrylate) matrix (PMMA) at 1, 5, and 10% (w/w), which revealed highly desirable photonic features. The Eu^{3+} and Gd^{3+} complexes were characterized by elemental and thermal analyses, in addition to ESI-MS spectrometry, FTIR, and Raman spectroscopy. Single-crystal X-ray diffraction studies of the tetrakis Bzim[Eu(tta)$_4$]·EtOH complex revealed that the $Bzim^+$ counteraction and EtOH molecules exhibited several intermolecular interactions with very short hydrogen bond distances between two $[Eu(tta)_4]^-$ anion units. The PMMA:(1%) Bzim[Eu(tta)$_4$]-doped material was thermally stable up to 120 °C, which was close to the values found for the Eu^{3+}-complex. Regarding the photoluminescence properties, either the Bzim[Eu(tta)$_4$]·H$_2$O or the doped films showed intense emission arising from the metal ion over a wide range of excitation wavelengths comprising UVA, UVB, and UVC regions. In addition, when the polymer films were exposed to sunlight radiation in an open external environment, the materials revealed a high Eu^{3+}-centered red emission arising from the $^5D_0 \rightarrow {}^7F_J$ transition. The Bzim[Eu(tta)$_4$]·H$_2$O and Bzim[Eu(tta)$_4$]·EtOH complexes showed high absolute quantum yields (Q^L_{Eu}) of 56% and 70%, respectively, whereas the doped polymer films displayed only ~38%. All materials exhibited a highly red monochromatic emission characteristic. We believe that such luminescent systems could be promising photonic materials with a wide excitation range, including UVA, UVB, UVC, and sunlight, acting as efficient light-converting molecular devices (LCMDs).

Received 6th September 2024
Accepted 1st November 2024

DOI: 10.1039/d4ra06451h

rsc.li/rsc-advances

Introduction

The search for renewable energy technologies has increased in the last decades as an alternative to the global dependency on fossil fuels, owing to their continuously rising prices and intrinsic environmental impacts, such as greenhouse gas emissions and global warming.[1–4] Although renewable source technologies based on solar energy are among the most widely investigated, their direct application for electricity generation in urban areas faces physical limitations owing to the reduced availability of space for installing photovoltaic panels in houses.[4,5] Alternatively, luminescent solar concentrators (LSCs) are a potential solution as they can be integrated into the building envelope or part of building components such as facades, roofs, windows, or noise barriers[5–7] owing to their intrinsic versatility for application under direct or diffuse radiation and without the requirement of sun tracking through lenses or mirrors.[8–10]

Among the considerable variety of fluorophores, such as fluorescent polymers, metallic and carbon nanoparticles, luminescent MOFs, biomolecules, as well as the particularly promising organic dyes, semiconductor nanocrystals (as quantum dots), and trivalent lanthanide (Ln^{3+}) based complexes, the latter presents some advantages over the former, such as large pseudo-Stokes-shift to prevent reabsorption losses and tunable absorption range (covering the visible/NIR spectral

---

[a] Department of Fundamental Chemistry, Institute of Chemistry, University of São Paulo, 05508-000 São Paulo, SP, Brazil. E-mail: ipassuncao@ifsp.edu.br

[b] Federal Institute of Education, Science and Technology of São Paulo, São Paulo, 01109-010, Brazil

[c] Nuclear and Energy Research Institute – IPEN/CNEN, 05508-000, São Paulo, SP, Brazil

[d] Institute of Chemistry of São Carlos, University of São Paulo, 13566-590, São Carlos, Brazil

[e] Department of Fundamental Chemistry, Federal University of Pernambuco, 50670-901, Recife, PE, Brazil

† Electronic supplementary information (ESI) available. CCDC 2380427. For ESI and crystallographic data in CIF or other electronic format see DOI: **https://doi.org/10.1039/d4ra06451h**

region) depending on the ligands and the selected Ln^{3+} ion.[11] Additionally, these complexes usually show high-emission quantum yield, good solubility in organic solvents, and compatibility with polymeric matrices, such as polymethylmethacrylate (PMMA).[11,12]

In the last decades, Ln^{3+}-based luminescent materials have been widely used in different areas such as optical markers,[13,14] medical diagnosis,[15,16] temperature sensors,[17,18] hybrid materials,[19,20] as well as LSCs.[8,21,22] Among them, the Eu^{3+} ion deserves special attention due to its inherent spectroscopic probe nature regarding the structural and intrinsic energy level structure. Such unique feature is mainly due to the ground ($^7F_0$) and first excited ($^5D_0$) states non-degeneracy, which greatly facilitates the interpretation of the experimental luminescence data.[23]

The inner nature of the 4f orbitals leads to essentially ionic interactions between the metal ion and a given ligand, in coordination complexes, for instance. Thus, the absorption and emission spectra of Ln^{3+} compounds present a line-like character, which usually shows highly monochromatic emissions. Nevertheless, intraconfigurational 4f transitions are forbidden by the Laporte rule, and lead to very low molar absorptivity coefficients. To overcome such drawbacks, the choice of appropriate organic ligands that are capable of absorbing and transferring the excitation energy to the Ln^{3+} ion is of paramount importance in designing highly efficient and luminescent coordination compounds.[24]

The most common intramolecular energy transfer process between the ligand and the Ln^{3+} ion usually occurs firstly *via* the strong ligand absorption from the ground to excited singlet states ($S_0 \rightarrow S_n$). Subsequently, the first excited S_1 state decays nonradiatively through intersystem crossing (ISC) to a lower triplet state ($S_1 \rightarrow T_1$). Finally, the excited T_1 state transfers the energy *via* a nonradiative path to the Ln^{3+} excited levels, which emits light according to its energy level structure.[24–26]

β-Diketonate Ln^{3+} complexes have found wide applications, mainly with the Eu^{3+} ion, due to their usually high molar absorptions and suitable T_1 state position for an efficient Eu^{3+} sensitization through the so-called antenna effect.[27] It is noteworthy that high energy oscillators like O–H, *e.g.*, from coordinated solvent molecules, can serve as an efficient channel for non-radiative luminescence quenching.[28–30] Such spectroscopic disadvantage can be overwhelmed by replacing these molecules for ancillary ligands or by a fourth ligand, giving rise to a tetrakis species $Q[Ln(\beta\text{-diketonate})_4]$.[31] In this last case, due to a negative net charge of the complex anion $[Ln(\beta\text{-diketonate})_4]^-$, a countercation ($Q^+$) must be present for electrical neutrality.

Organic polymers usually present desirable features for application purposes like versatility, mechanical strength, relatively low cost of production, and flexibility.[20,32] The PMMA polymer is one of the most widely used mainly due to its excellent mechanical and optical properties,[20] besides high light transmittance, chemical resistance, and low optical absorption.[19] Thus, additional synergistic properties can be achieved by doped luminescent materials, such as Eu^{3+}-β-diketonate complexes into a PMMA matrix,[19,20,32–36] as well as other matrices.[37,38]

This work investigated the synthesis and characterization, as well as spectroscopic features of the benzimidazole tetrakis(2-thenoyltrifluoroacetonato)europate(III) and gadolinite(III) complexes, $Bzim[Eu(tta)_4]\cdot H_2O$. Additionally, the Eu^{3+}-complex was incorporated into PMMA polymeric films in 1, 5, and 10% (w/w), and showed intense red emission arising from the $^5D_0 \rightarrow {}^7F_2$ transition of the Eu^{3+} ion under excitation at 254, 380, and 405 nm, and when exposed to sunlight irradiation. This work also aims to contribute toward a deeper understanding of the chemical interactions involving the complex and the host matrix *via* a detailed vibrational investigation through FTIR and FT-Raman spectroscopy, as well as in the matter of photophysical parameters (intensity parameters, radiative and non-radiative rates, intrinsic and absolute quantum yields) of the complex itself and the doped materials. Such experimental results suggest the possible application of these materials as light-converting molecular devices (LCMDs).

Experimental

The Ln^{3+} nitrate salts (Ln^{3+} = Eu and Gd) were synthesized in accordance with the literature[39] by the reaction of the corresponding oxide (Ln_2O_3) with HNO_3 concentrated acid. Subsequently, the $Ln(NO_3)_3\cdot 6H_2O$ aqueous solution was filtered using filter paper and a regular funnel under ordinary pressure. The solvent was then evaporated, leading to a crystalline solid that was subsequently dried and stored under reduced pressure.

The $Bzim[Ln(tta)_4]$ complex (Ln^{3+} = Eu and Gd), whose molecular structure can be seen in Fig. 1, was synthesized *via* one-pot synthesis containing 0.86 mmol of $Ln(NO_3)_3\cdot 6H_2O$, 4.33 mmol of thenoyltrifluoroacetone (Htta) ligand and 0.86 mmol of benzimidazole, Bzim, in an isopropanol (*ca.* 30 mL) solution. The Htta ligand was previously deprotonated with a concentrated ammonia solution until a pH ∼ 7 was achieved. The $Ln(NO_3)_3\cdot 6H_2O$ solid was dissolved in 1.0 mL of water, and slowly added to the tta/Bzim homogeneous mixture in the Ln^{3+} : Htta : Bzim molar ratio of 1 : 5 : 1. The reactional mixture was kept under stirring for 2 h without heating. After that, the formed heterogeneous mixture was filtered with filter paper under ordinary pressure with a regular funnel, washed with small portions (*ca.* 10 mL) of cold isopropanol, dried in the oven at 50 °C, and stored in a desiccator under vacuum. Then, the tetrakis $Bzim[Ln(tta)_4]$ complexes were obtained as a powder,

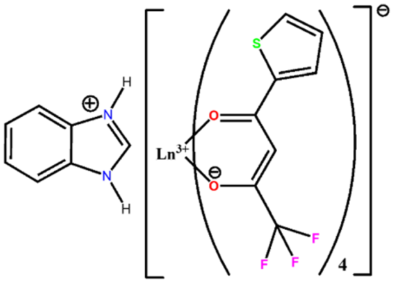

Fig. 1 Structural formula of the tetrakis $Bzim[Ln(tta)_4]$ complex, where Ln^{3+} = Eu and Gd.

showing the general formula Bzim[Ln(tta)$_4$]·H$_2$O (presented an off-white color). The Eu^{3+} complex was obtained as suitable single crystals for X-ray measurements after recrystallization with 15 mL of ethanol (presenting a light orange color). These Ln^{3+} complexes are soluble in different solvents, such as methanol, ethanol, acetone, CHCl$_3$, DMSO, MeCN, and THF, as well as hot isopropanol. The percent yield for the reactions was about 85%.

The incorporation of the luminescent Eu^{3+} β-diketonate complex into the PMMA matrix was achieved by the complete dissolution of 500 mg of solid PMMA and 5.0 mg of the Bzim[Eu(tta)$_4$]·H$_2$O compound in 50 mL of acetone with stirring at 60 °C for 1 hour. Afterward, the resulting solution was poured onto a Petri dish and further heated at 60 °C, leading to a transparent polymeric film[22] after complete evaporation of the solvent. The same procedure was adopted for all concentrations of the Eu^{3+} complex under consideration in this study. The PMMA-doped films were labeled according to the concentration of the Bzim[Eu(tta)$_4$]H$_2$O complex as PMMA:(x%)Bzim[Eu(tta)$_4$], where $x = 1$, 5 and 10% (w/w), respectively.

The elemental analyses were performed in PerkinElmer CHN 2400 instruments. The infrared absorption spectra were obtained using an equipment Bruker Vertex 80 V IR spectrometer equipped with a vacuum system in the sample compartment. The spectra were acquired under ATR (attenuated total reflectance) mode in the low (125–675 cm^{-1}) and high-frequency (400–4000 cm^{-1}) ranges. A small amount of the sample was powdered into fine grains, and then placed on the diamond crystal of the ATR accessory; the sample chamber was held under vacuum (~2 mbar). The spectra were recorded from an average of 256 scans, with a spectral resolution of 2.0 cm^{-1}. Raman spectra were measured in a Bruker Multi-RAM FT-Raman spectrometer using a Nd^{3+}:YAG laser as the light source (λ = 1064 nm). The spectra were acquired in the frequency range from 150 to 4000 cm^{-1}. Thermogravimetric analysis (TG) was performed in the 25 to 950 °C range on a 2950 TGA HR V5.4 A under a dynamic synthetic air atmosphere of 50 cm^3 min^{-1} with a constant heating rate of 10 °C min^{-1}. Single crystal X-ray diffraction data of the Bzim[Ln(tta)$_4$]·EtOH complex were collected on a BRUKER diffractometer – model APEX II Duo with Mo-Kα radiation (λ = 0.71073 Å). Data reduction and absorption correction were performed using standard procedures. The structure of the complex was predicted by direct methods and refined using SHELXS-97,[40] and all non-hydrogen atoms were refined with anisotropic displacement parameters using SHELXL2014. The positions of the hydrogen atoms were calculated using the riding model option in SHELXL2014.[41] The crystallographic refinement parameters are presented in Table S1,† and the crystal structure of Bzim[Eu(tta)$_4$]·EtOH was deposited in the Cambridge Structural Database with the code CCDC 2380427. Powder X-ray diffraction patterns were obtained with a Miniflex Rigaku diffractometer using Cu Kα$_1$ radiation (30 kV and 15 mA) in the (2θ) 5–80° range and with 0.05 s of pass time. The excitation and emission spectra of the Ln^{3+} complexes in solid state at room (300 K) and liquid nitrogen (77 K) temperatures were recorded at an angle of 22.5° (front face) with a spectrofluorometer (SPEX-Fluorolog 3) with double grating between 0.5 and 2.0 mm monochromator (SPEX1680), and the excitation source was a 450 W Xenon lamp. All spectra were recorded using a detector mode correction. Moreover, the luminescence decay curves of the emitting levels of the Eu^{3+} ion complex and the PMMA-doped films were obtained at room temperature, using a phosphorimeter SPEX 1934D accessory coupled to the spectrofluorometer. The emission spectra of the Bzim[Ln(tta)$_4$] complex and the corresponding PMMA-doped films under sunlight irradiation were recorded using an Ocean Optics fiber optics (diameter 1 mm) connected to an Ocean Optics QE65000 spectrometer with resolution up to 1 nm. Photoluminescence quantum yield measurements (PLQYs) of the Ln^{3+} complexes and PMMA-doped film were recorded in solid state using an Edinburgh FS5 Spectrofluorometer equipped with a SC-30 Integrating Sphere. All compounds were excited under $\lambda_{\mathrm{exc}} = 360$ nm and the photoluminescence emission was monitored in the spectral range of 330–725 nm, applying an integration time of 0.5 seconds and a step of 0.5 nm, with a slit width of 3 nm for excitation and 0.5 nm for the emission at ~300 K.

Results and discussion

The experimental and calculated elemental analysis data (CHN) of the complexes showed good agreement between each other, *i.e.*, Bzim[Eu(tta)$_4$]·H$_2$O: theoretical for C$_{39}$H$_{23}$EuF$_{12}$N$_2$O$_8$S$_4$: C 39.91, H 2.15, N 2.39%; found: C 39.78 H 2.04, N 2.20%; Bzim[Gd(tta)$_4$]·H$_2$O: theoretical for C$_{39}$H$_{23}$GdF$_{12}$N$_2$O$_8$S$_4$: C 39.73, H 2.14, N 2.38%; found: C 39.89, H 2.03, N 2.59%, and Bzim[Eu(tta)$_4$]·EtOH: theoretical for C$_{41}$H$_{31}$EuF$_{12}$N$_2$O$_9$S$_4$: C 40.91, H 2.60, N 2.33%; found: C 40.24, H 2.20, N 2.60%. These results suggest the formation of the tetrakis [Ln(tta)$_4$]$^-$ species stabilized with benzimidazolium (Bzim$^+$) as a counteraction. Interestingly, the product obtained immediately after precipitation leads to the formation of complexes containing a water molecule in its structure, *i.e.*, Bzim[Eu(tta)$_4$]·H$_2$O. Meanwhile, the product obtained from recrystallization in ethanol favours the formation of a complex containing one EtOH molecule in its structure, giving rise to the Bzim[Eu(tta)$_4$]·EtOH formula. The ESI(+) MS data (Fig. S1†) for the Bzim[Eu(tta)$_4$]·H$_2$O complex revealed an intense peak at m/z = 119.0613 (theor. m/z = 119.0609) arising from the Bzim$^+$ cation, while the ESI(−) MS revealed m/z = 1036.8715 (theor. m/z = 1036.8749) for the [^{153}Eu(tta)$_4$]$^-$ anionic species (Fig. S2†).

To gain a deeper understanding of the structure and possible interactions between the host PMMA matrix and the Bzim[Eu(tta)$_4$]·H$_2$O, powder X-ray diffraction measurements were carried out between 5 and 80° at room temperature (Fig. S3†). The Eu^{3+} complex samples revealed a crystalline profile either for the one containing H$_2$O or an EtOH molecule, with the most intense peak at 20.5 and 8.7°, respectively. On the other hand, the polymeric matrix spectral profile revealed an amorphous character, in contrast to the complexes profile. However, the diffraction patterns of the polymers are very similar among each other, irrespective of the complex concentration and even for the undoped film. This suggests that no significant structural modification of the polymers occurred upon doping, and that the doped compounds are solvated into the polymer and not crystallized.

Single crystal X-ray analysis of Bzim[Eu(tta)$_4$]·EtOH reveals that the compound crystallizes in the $P2_1/c$ space group, where each asymmetric unit contains [Eu(tta)$_4$]$^-$ anions interacting with the Bzim$^+$ cation and one EtOH molecule, involving strong intermolecular hydrogen bonding (Fig. 2a and S3a†). The Bzim$^+$ countercation is positioned between two units of the [Eu(tta)$_4$]$^-$ anion. It is interesting to observe that the H1A, H2A, and H33 hydrogen atoms of the imidazolium ring form hydrogen bonds with two units of [Eu(tta)$_4$]$^-$ anion, and one EtOH molecule. As shown in Fig. 2a, the coordinated oxygen atoms (O3, O6, and O7) from the tta ligand form hydrogen bonds with Bzim$^+$ (H1A, H2A, and H39), and the O4 atom from tta forms a hydrogen bond with one lattice EtOH molecule (O4···H9A). Furthermore, the oxygen atom from the EtOH molecule interacts with a Bzim cation (O9···H33). The Bzim cation also presents the hydrogen bond with fluorine atoms from the CF$_3$ moiety in the tta ligand.

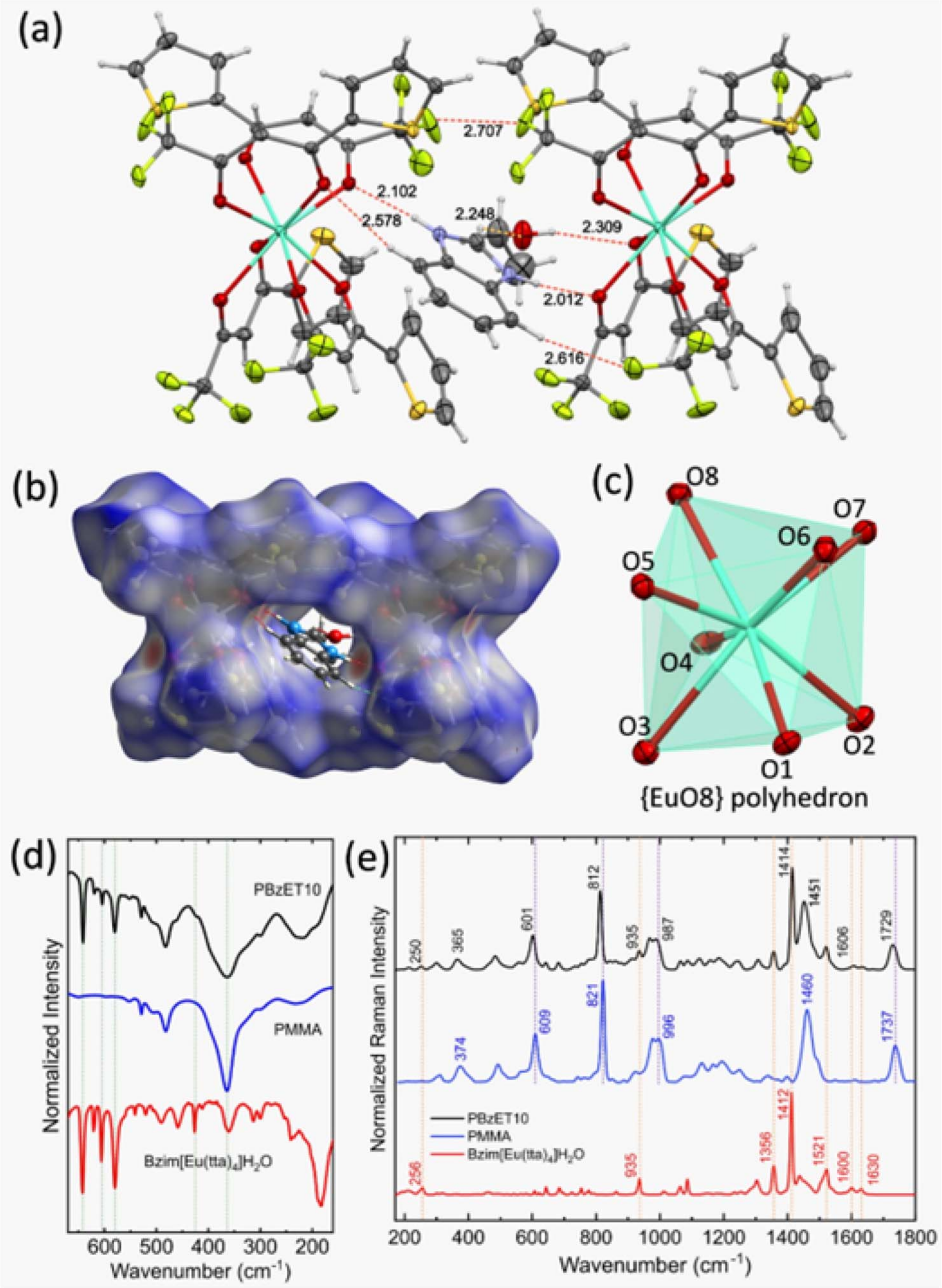

Fig. 2 (a) Crystal structure of the Bzim[Eu(tta)$_4$]·EtOH with ellipsoids at 50%, highlighting the hydrogen bonds (dashed orange lines) among the Bzim$^+$ counterion, two [Eu(tta)$_4$]$^-$ anions, and one EtOH molecule. (b) Hirshfeld surfaces mapped with d_{norm} for Bzim$^+$ and two [Eu(tta)$_4$]$^-$ anion interaction in the crystal packing. (c) Coordination polyhedron formed by eight oxygen atoms in a triangular dodecahedron. (d) Far-FTIR spectra recorded from 670 to 150 cm^{-1} (d) and FT-Raman spectra with 1064 nm excitation laser (e) for the Bzim[Ln(tta)$_4$]·H$_2$O complex (red line), undoped PMMA polymer (blue line), and PMMA:(10%)Bzim[Eu(tta)$_4$]-doped film (black line).

Such hydrogen bonds involving the countercation and oxygen atoms from the tta ligands in tetrakis europium complexes have been reported in a system containing an imidazolium-based countercation and $[Eu(tta)_4]^-$.[42] The coordination environment surrounding the Eu^{3+} center is octa-coordinated by eight oxygen atoms from the four tta ligands. Remarkably, each of the Eu–oxygen bond distance is distinct, ranging from 2.344 to 2.454 Å, leading to a distorted polyhedron $\{EuO_8\}$ that is characterized as a triangular dodecahedron with D_{2d} symmetry site (TDD-8, $S = 0.913$), giving by Shape 2.1 program[43] (Fig. 2c).

Furthermore, the main intermolecular interactions were represented by Hirshfeld surface analysis (Fig. 2b and S3b†) to quantify and visualize the closed intermolecular contacts from the crystal structure of $Bzim[Eu(tta)_4]\cdot EtOH$. Thus, the electron density in the red region is relatively high due to the presence of hydrogen bonds, leading to intermolecular packing, whereas the electron density in the blue region is low due to the absence of such interactions.[44,45] The map in Fig. 2b is related mainly to close contacts between the Bzim cation and two $[Eu(tta)_4]^-$ anions units by strong H⋯O interactions, and also considers the H⋯F and C⋯H type interactions. Fig. S5† depicts the two-dimensional fingerprint plots that decompose to highlight these different intermolecular interactions and their contributions to the Hirshfeld surface area.

FTIR absorption spectra of the $Bzim[Ln(tta)_4]\cdot L$ compounds (Ln^{3+} = Eu and Gd, and L: H_2O or EtOH) and PMMA:(x%)Bzim$[Eu(tta)_4]$ (x = 1, 5 and 10) were recorded in the mid-infrared (MIR) 4000–400 cm^{-1} and Far-infrared (FIR) 670–150 cm^{-1} ranges (Fig. S6–S8†). The smooth broad band from the 3600 to 3000 cm^{-1} range suggests the presence of an H_2O or EtOH molecule in the complexes (Fig. S6†). The characteristic strong narrow absorption peak at 1658 cm^{-1}, ascribed to the C=O stretching mode in free Htta ligand, is shifted to lower frequencies (1595 cm^{-1}) in the complexes.[46] This indicates the coordination of the tta ligand to the metal ion through a bidentate chelate mode.[47] The presence of a single sharp and intense peak at 1354 cm^{-1} in the complexes (Fig. S6†), in contrast to the peaks at 1365 and 1345 cm^{-1} arising from the C–N mode in the free benzimidazole,[48,49] indicates the presence of the $Bzim^+$ cation in the $Bzim[Eu(tta)_4]\cdot H_2O$ complex. This result is in good agreement with the ESI(+) MS and single crystal X-ray analyses. In addition, FTIR spectra for the $Bzim[Eu(tta)_4]\cdot EtOH$ compound present a similar absorption profile, suggesting that the substitution of the water molecule by one EtOH does not lead to any significant structural changes. The FTIR spectra of the doped PMMA films proved that the incorporation of the tetrakis $Bzim[Eu(tta)_4]$ complex into the PMMA matrix was successfully carried out. Thus, the main bands assigned to the complex can be seen in the doped films, even at low frequencies (670–150 cm^{-1}). The Far IR spectra in Fig. 2d (Fig. S8†) indicate that the absorption bands of PMMA and the pure tetrakis complex appear in the same spectral region for the doped PMMA film, indicating that the structure of the complex was preserved. In addition, some absorption bands of the PMMA polymer experience a broadening after the incorporation of the complex.

The FT-Raman data provide the most effective insights into the effect of incorporating the complex in the PMMA polymer (Fig. 2e and S9†). Interestingly, we can observe a shift of different bands from the complex to higher and lower frequencies after the incorporation into the polymer matrix. While PMMA bands shift to lower frequencies at doped PMMA, *e.g.*, the bands ascribed to the C–O–C symmetric stretching (996 cm^{-1}), O–CH_3 bending vibration (1460 cm^{-1}) and C=O symmetric stretching (1737 cm^{-1}) of the PMMA shift to 987, 1451, and 1729 cm^{-1} in PMMA:(x%)Bzim$[Eu(tta)_4]$ (x = 1, 5 and 10). This indicates a mutual influence of the tetrakis complex upon the chemical environment of the PMMA matrix and a joint polymer–complex interaction.[50]

The thermal behaviour (Fig. 3) of the $Bzim[Eu(tta)_4]\cdot L$ complexes, L: EtOH or H_2O, shows that the first event corresponds to the release of one crystallization ethanol molecule (0.8% loss/50–65 °C) or H_2O (2.30% loss/90–125 °C) stabilized by hydrogen bonding through the N atom of the $Bzim^+$ counteraction and $[Eu(tta)_4]^-$ anion. The second and third steps of decomposition in the complexes are very similar, where the second step takes place from nearly 140 to 350 °C accounting for ~60% of the weight loss. Subsequent events are all overlapped and correspond to thermal decompositions in the 350 to 570 °C and 570 to 800 °C intervals, corresponding to 19.7 and 1.35% of mass loss, respectively. The final residue from the decomposition of the $Bzim[Eu(tta)_4]^-H_2O$ complex is indicated to be EuOF, as its experimental remaining mass percentage (16.8%) resembles the theoretical one (16.2%). On the other hand, the TG curves of the PMMA:(1%)Bzim$[Eu(tta)_4]$ and undoped PMMA polymer showed a distinct decomposition pattern and an almost complete mass consumption when compared to the corresponding Eu^{3+} complex. The weight loss takes place in two and one events, respectively, for the PMMA samples with and without Eu^{3+} complex doping. The initial degradation

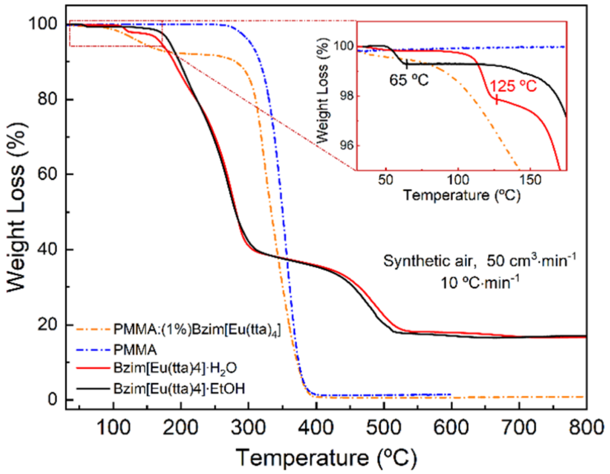

Fig. 3 Thermogravimetric curves of the $Bzim[Eu(tta)_4]\cdot H_2O$ and Bzim$[Eu(tta)_4]\cdot EtOH$ complexes (solid red and black lines), PMMA:(1%)Bzim$[Eu(tta)_4]$-doped film (dashed orange line), and undoped PMMA polymer (dashed blue line). All curves were obtained under a dynamic synthetic air atmosphere of 50 cm^3 min^{-1} with a constant heating rate of 10 °C min^{-1} from 25 to 800 °C.

temperature of the undoped PMMA is decreased from nearly 280 to 120 °C in the doped film, possibly due to residual solvent molecules. Such thermal behaviour was also observed in other Eu^{3+}-β-diketonate molecules doped in polymer films.[51] The final decomposition event (beginning around 430 °C) for both PMMA systems indicates the same thermal feature. In general, the TG experimental data corroborate with the elemental analysis.

Photophysical properties

Phosphorescent behaviour of Bzim[Gd(tta)$_4$] complex. An analogous Bzim[Gd(tta)$_4$]·H_2O complex was also synthesized to obtain information on the relative position of the T_1 state from the tta ligand. It is noteworthy that the Gd^{3+} has an ionic radius very similar to that of the Eu^{3+} ion, which can mimic the chemical environment around the europium ion.[52,53] Moreover, the Gd^{3+} ion presents no optical activity above 315 nm due to the large energy gap between the $^8S_{7/2}$ ground state and its first $^6P_{7/2}$ excited state (31 700 cm^{-1});[54] thus avoiding the energy transfer from the organic ligand triplet states. To prevent possible contributions from the $S_1 \rightarrow S_0$ transition, the time-resolved phosphorescence spectrum of the solid-state Bzim[Gd(tta)$_4$]·H_2O complex (Fig. 4) was recorded at 77 K in the range from 425 to 725 nm under excitation at 380 nm with a delay of 1.0 ms.

Usually, the T_1 state energy position of the ligand can be determined by the phosphorescence broad band of the Ln^{3+} complexes (Ln^{3+}: La, Gd, or Lu) in two main ways: (i) the so-called zero-phonon transition (the higher energy side of the phosphorescence band) and (ii) the barycenter of this band.[55] In this work, we avoid using the band's barycenter due to the T_1 state energy being positioned between the $^5D_1$ (18 970 cm^{-1}) and $^5D_0$ (17 230 cm^{-1}) excited levels of the Eu^{3+} ion. Such a procedure would lead to a significant contribution of the back energy transfer process, and consequent strong luminescence quenching. Therefore, we used the zero-phonon energy of the phosphorescence broad band of the Bzim[Gd(tta)$_4$]·H_2O complex (Fig. 4) to assign the T_1 state of the tta ligand at 20 830 cm^{-1}. This optical feature suggests that the $T_1 \rightarrow Eu^{3+}$ intramolecular energy transfer process plays a significant role in the luminescence sensitization, as will be further discussed in the following section.

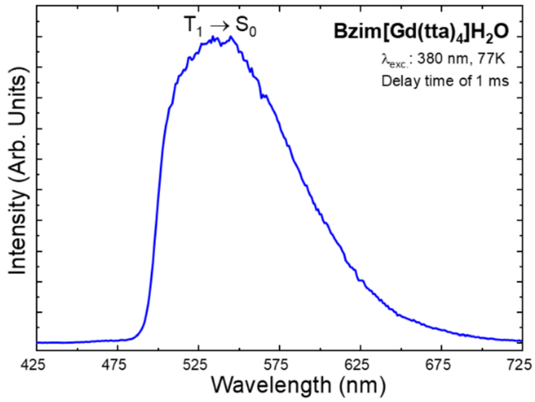

Fig. 4 Phosphorescence spectrum of the solid-state Bzim[Gd(tta)$_4$]·H_2O complex recorded at 77 K from 425 to 725 nm under excitation at 380 nm with 1.0 ms of delay.

Photoluminescent investigation of PMMA films doped with the Bzim[Eu(tta)$_4$]H_2O complex. The excitation spectra of the PMMA:(x%)Bzim[Eu(tta)$_4$] films (x = 1, 5 and 10%) and the complex were registered from 250 to 600 nm at 300 K, monitoring the emission under the $^5D_0 \rightarrow {}^7F_2$ transition (612 nm) of the Eu^{3+} ion (Fig. 5). The excitation spectrum of the solid-state europium complex revealed an intense broad band in the 250 to 500 nm range, assigned to the $S_0 \rightarrow S_n$ transition centered on the tta ligand. In addition, it is possible to observe narrow peaks centered at 464 (overlapped), 526, 578, and 535 nm, and assigned to the $^7F_0 \rightarrow {}^5D_{2,1,0}$ and $^7F_1 \rightarrow {}^5D_1$ transitions of the from Eu^{3+} ion, respectively.[23]

The excitation spectrum of the Eu^{3+} complex at 77 K (Fig. S10a and b†) was also registered under the same experimental conditions as the room temperature ∼300 K one (Fig. 5), and revealed a similar spectral profile, except for a higher resolution and a considerably lower intensity of the $^7F_1 \rightarrow {}^5D_1$ transition at low temperature (77 K). Such a result is due to the small energy gap between the $^7F_0$ ground state and $^7F_1$ first excited level (∼380 cm^{-1}),[23] indicating that the $^7F_1$ energy level can be thermally populated.

On the other hand, the excitation bands of the PMMA:(x%)Bzim[Eu(tta)$_4$] films (Fig. 5) are very similar among the different Eu^{3+} complex concentrations (x = 1, 5, and 10%), and significantly different compared to the Bzim[Eu(tta)$_4$]·H_2O spectral profile. It is noteworthy that the PMMA-doped materials showed a rather lower intensity of the 4f–4f transitions from the Eu^{3+} ion in comparison with the complex. This is due to the low concentration of the metal ion in the doped material.

Emission spectra of the Bzim[Eu(tta)$_4$]·H_2O complex and the PMMA doped films were also recorded at 300 K in the 550 to 750 nm range under excitation on the ligand band at 380 nm

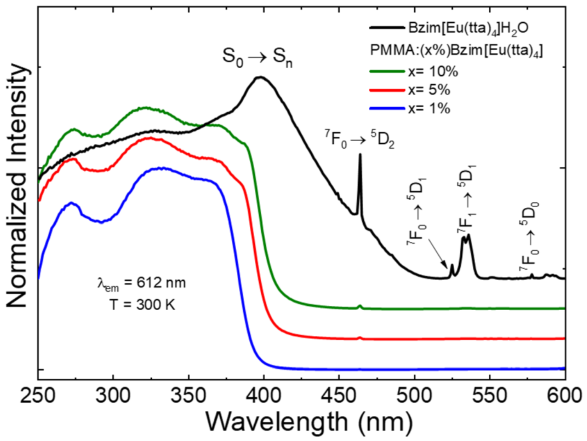

Fig. 5 Excitation spectra of the solid state Bzim[Eu(tta)$_4$]·H_2O complexes and the corresponding PMMA:(x%)Bzim[Eu(tta)$_4$]-doped films, for which x = 1, 5 and 10% (w/w). All excitation spectra were recorded under room temperature in the 250–600 nm range, monitoring the emission at the hypersensitive $^5D_0 \rightarrow {}^7F_2$ transition ($\lambda_{em.}$ = 612 nm) of the Eu^{3+} ion.

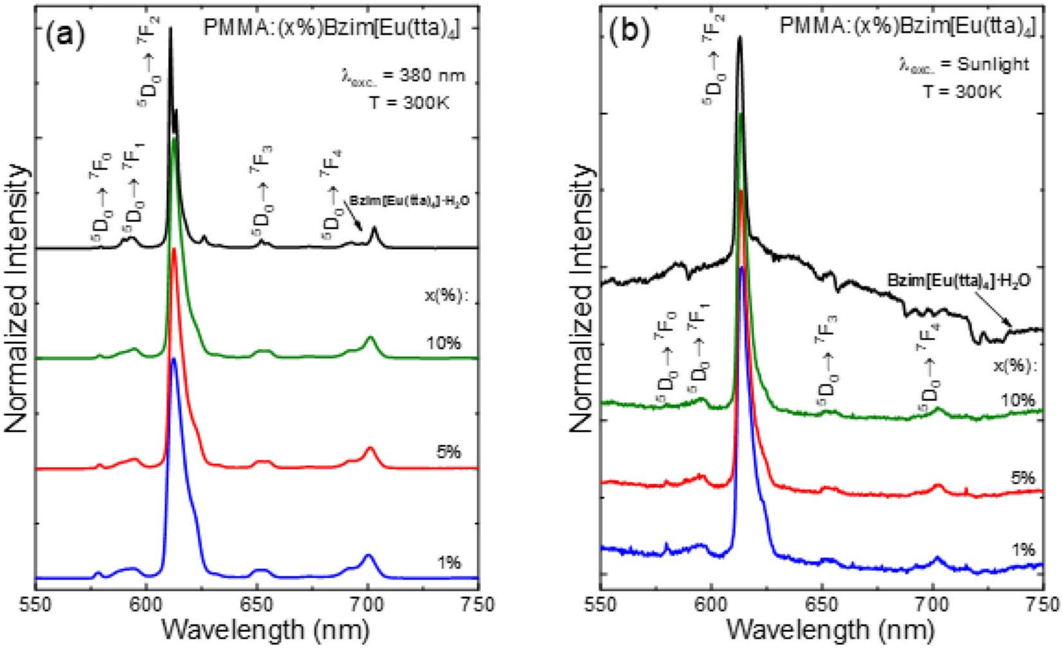

Fig. 6 Emission spectra of the Bzim[Eu(tta)$_4$]·H$_2$O complex (black line) and the doped PMMA:(*x*%)Bzim[Eu(tta)$_4$] polymers, where $x = 1\%$ (blue line), 5% (red line) and 10% (green line) with excitation at 380 nm (a) and under sunlight exposure (b). All spectra were recorded at room temperature in the range of 550 to 750 nm.

(Fig. 6a), as well as under sunlight exposure (Fig. 6b). These optical data revealed no broad emission bands arising from the tta moiety, suggesting an efficient L → Eu^{3+} energy transfer. Yet, the low-temperature spectra (Fig. S11a and b†) showed better spectral resolution due to lower vibronic contributions, and the most intense transition is the $^5D_0 \rightarrow {}^7F_2$ one at 612 nm for both temperatures. The doped polymeric film spectra showed similar emission profiles that were distinct from the Eu^{3+}-complex sample regarding the bandwidths. Nevertheless, for all samples, only characteristic narrow emission peaks attributed to intraconfigurational $^5D_0 \rightarrow {}^7F_J$ ($J = 0, 1, 2, 3,$ and 4) transitions of the Eu^{3+} ion were observed at 579, 592, 612, 653, and 703 nm, respectively. The most intense peak corresponds to the $^5D_0 \rightarrow {}^7F_2$ transition that accounts for the main process responsible for the high red emission of these materials. However, the emission peaks of the PMMA-doped films are broader than those of the Eu^{3+} complex ones due to polymeric system features.

Interestingly, the emission profile of the doped polymeric films is practically the same as each other, yet quite different from that of the complex powder. This feature suggests the presence of the tetrakis complexes, where the PMMA polymer acts more like a solvent, and the emission is the broadened profile of a [Eu(tta)$_4$]$^-$ anion moiety. Indeed, one can see that the doped polymer emission bands are very similar to solutions of [Eu(tta)$_4$]$^-$ with different cations, as previously reported by Blois *et al.*[42]

Fig. 6b exhibits the emission spectra of the complex in the solid state, as well as the corresponding PMMA:(*x*%)Bzim[Eu(tta)$_4$] doped films ($x = 1$, 5 and 10%) at 300 K when directly exposed to sunlight radiation by using an Ocean Optics QE65000 spectrometer coupled with an optical fiber. An important spectroscopic feature of the doped film emission spectra is the absence of broadband arising from the solar background radiation observed in the Bzim[Eu(tta)$_4$]$^-$·H$_2$O complex. For the emission spectra obtained under excitation by the sunlight radiation, only $^5D_0 \rightarrow {}^7F_{0-4}$ transitions from the Eu^{3+} were observed. This shows the most intense one also as the $^5D_0 \rightarrow {}^7F_2$ transition at around 612 nm, which is thus the main process responsible for the intense red emission of the films in an external environment even on cloudy days.

The experimental intensity parameters (Ω_2 and Ω_4) values were calculated for the Bzim[Eu(tta)$_4$]·H$_2$O complex and the PMMA:(*x*%)Bzim[Eu(tta)$_4$]-doped films, according to eqn (1):

$$A_{0\rightarrow J} = \frac{4\omega^3 e^2 \chi}{3\hbar c^3}\Omega_\lambda \left|\left\langle {}^5D_0 \| U^{(\lambda)} \| {}^7F_\lambda \right\rangle\right|^2 \quad (1)$$

in which ω is the angular frequency of the transition, e is the elementary charge, χ is the Lorentz local field correction factor, $\hbar$ is the reduced Planck's constant, and c is the speed of light. The $|\langle {}^5D_0 \| U^{(\lambda)} \| {}^7F_\lambda \rangle|^2$ quantities represent the squared reduced matrix elements, for which the values are equal to 0.0032 and 0.0023 for $\lambda = 2$ and 4, respectively.[56,57]

In general, the index of refraction (n) for the Eu^{3+} complexes is used as 1.5.[55] Recent studies revealed that the Ω_2 values are more sensitive to even small angular variations, while the Ω_4 values are much more sensitive to the ligating atom-Eu^{3+} ion distance variations (covalent character).[58,59] Moreover, the experimental values for the spontaneous emission coefficients ($A_{0\rightarrow J}$) related to the $^5D_0 \rightarrow {}^7F_{0\rightarrow 4}$ transitions of the Eu^{3+} ion were determined from the room temperature emission spectra of the Bzim[Eu(tta)$_4$]·H$_2$O complex and doped films *via* eqn (2):[24,57,60]

$$A_{0\to J} = \left(\frac{S_{0\to J}}{S_{0\to J}}\right) A_{0\to 1} \tag{2}$$

where $S_{0\to 1}$ and $S_{0\to J}$ correspond to the areas under the emission curves of the $^5D_0 \to {}^7F_1$ and $^5D_0 \to {}^7F_{2,4}$, respectively. Additionally, the $^5D_0 \to {}^7F_1$ transition is almost entirely governed by the magnetic dipole (MD) mechanism and its intensity is practically insensitive ($n = 1.5$, $A_{0\to 1} \sim 50\ \mathrm{s}^{-1}$)[60] to the chemical environment around the Eu^{3+} ion. Thus, this transition is often used as an internal reference.

The intrinsic emission quantum yield (Q^{Eu}_{Eu}) in eqn (3) is defined as the ratio between the radiative (A_{rad}) and the total (A_{total}) decay rates, with the total rate being the sum of the radiative and non-radiative (A_{nrad}) rates.[55,60] Moreover, the A_{total} rate is related to the emitting level lifetime (τ_{obs}) by eqn (4),[48] in which the τ_{obs} values were calculated from the luminescence decay curves obtained under excitation at the $^7F_0 \to {}^5D_2$ transition (464 nm) and registered at room temperature for the Eu^{3+} complex and the doped PMMA films (Fig. S12†) to calculate the Q^{Eu}_{Eu} values.

$$Q^{Eu}_{Eu} = \frac{A_{rad}}{A_{rad} + A_{nrad}} = \frac{\tau_{obs}}{\tau_{rad}} \tag{3}$$

$$\tau_{obs} = \frac{1}{A_{rad} + A_{nrad}} = \frac{1}{A_{total}} \tag{4}$$

The Ω_2 values of the Bzim[Eu(tta)$_4$]·H_2O complex and the doped PMMA polymer films (Table 1) are very high for both systems, reflecting the high relative intensity of the $^5D_0 \to {}^7F_2$ transition of the Eu^{3+} ion and its hypersensitive nature.[61,62] In addition, the Ω_2 values for the doped PMMA films are higher than for the complex, and decrease as the concentration increases. The Ω_2 parameter decreases as the concentration increases, owing to the lower angular distortions (Table 1). Such an optical feature is possibly a consequence of an increase in the hydrogen interactions between the N atom of the $Bzim^+$ counterion and the oxygen atom from the PMMA matrix as the doping concentration increases. The Ω_4 values for the doped films are higher than that of the Eu^{3+}-complex. However, the values are very similar (Table 1), indicating a less covalent character for the complex.

Actually, the overall quantum yield (Q^{L}_{Ln}) should be lower than the intrinsic quantum yield (Q^{Ln}_{Ln}) for the Ln^{3+} materials. Table 1 shows that the Q^{L}_{Eu} values for the hydrated Eu^{3+} complex and doped systems are lower than those of Q^{Eu}_{Eu}, as expected. However, the overall quantum yield value of the Bzim[Eu(tta)$_4$]·EtOH complex is much higher than the intrinsic quantum yield, in the margin of error. When the intrinsic and overall quantum yield values are similar, it suggests an efficient tta → Eu energy transfer. Additionally, the Q^{L}_{Eu} and Q^{Eu}_{Eu} values are higher for Bzim[Eu(tta)$_4$]·EtOH than the hydrated complex. However, this is explained by the single-crystal structure of Bzim[Eu(tta)$_4$]·EtOH, which shows that the solvent molecules are not coordinated to the central ion. Thus, their well-known vibronic quenchings are not operatives. Furthermore, the substitution of water by ethanol molecules during recrystallization is seen as it changes the 4f–4f intensity parameters of the europium(III) ion even though they are outside the first coordination sphere, showing the range sensibility of the europium ion. This corroborates that the Eu^{3+} ion acts as a powerful spectroscopic probe.[37,63]

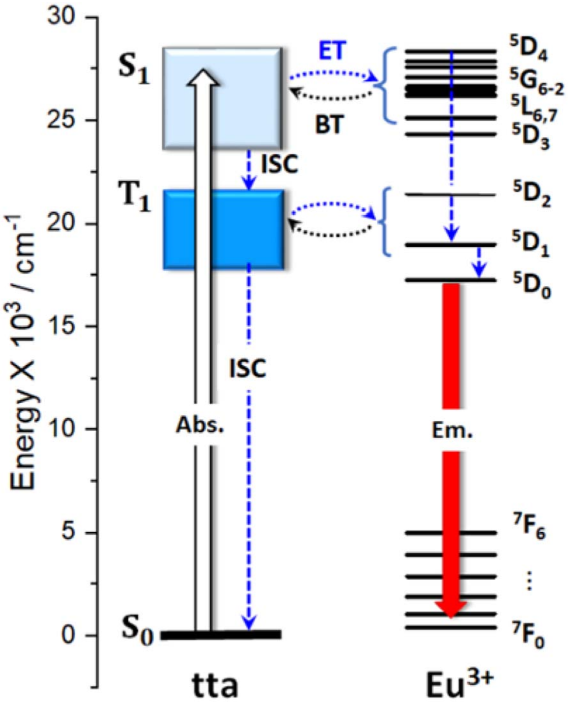

Fig. 7 Partial energy level diagram of the Bzim[Eu(tta)$_4$]·H_2O complex. The emission arises from the $^5D_0$ emitting level. S_0 and S_1 are the ligand ground and lowest singlet excited states, respectively. T_1 is the lowest triplet ligand level, Abs. is the initial absorption, ISC is the intersystem crossing, where Em. is the emission. ET and BT are the forward and backward energy transfer rates, respectively.

Table 1 Experimental intensity parameters ($\Omega_{2,4}$), radiative (A_{rad}) and non-radiative (A_{nrad}) decay rates, emission lifetime (τ_{464}), and intrinsic quantum yield (Q^{Eu}_{Eu}) of the solid state Bzim[Eu(tta)$_4$]·H_2O complex and the PMMA:(x%)Bzim[Eu(tta)$_4$] doped films (x = 1, 5 and 10%). All data were obtained at 300 K

Sample	Ω_2 (10^{-20} cm^2)	Ω_4 (10^{-20} cm^2)	A_{rad} (s^{-1})	A_{nrad} (s^{-1})	A_{total} (s^{-1})	τ_{obs} (ms)	Q^{Eu}_{Eu} (%)	Q^{L}_{Eu} (%)
Bzim[Eu(tta)$_4$]·EtOH	29.8 ± 1.3	2.92 ± 0.55	989 ± 39	585 ± 40	1572 ± 5	0.636 ± 0.001	63 ± 2	65 ± 7
Bzim[Eu(tta)$_4$]·H_2O	18.6 ± 1.0	2.90 ± 0.51	653 ± 45	542 ± 48	1195 ± 6	0.837 ± 0.001	55 ± 8	55 ± 6
PMMA:(1%)Bzim[Eu(tta)$_4$]	39.2 ± 1.5	7.26 ± 0.41	1330 ± 46	1326 ± 50	2656 ± 15	0.376 ± 0.001	50 ± 2	29 ± 3
PMMA:(5%)Bzim[Eu(tta)$_4$]	37.9 ± 1.0	7.52 ± 0.35	1299 ± 31	711 ± 32	2010 ± 10	0.497 ± 0.001	65 ± 2	38 ± 4
PMMA:(10%)Bzim[Eu(tta)$_4$]	36.9 ± 1.2	8.12 ± 0.43	1274 ± 37	769 ± 38	2043 ± 80	0.489 ± 0.001	62 ± 2	39 ± 4

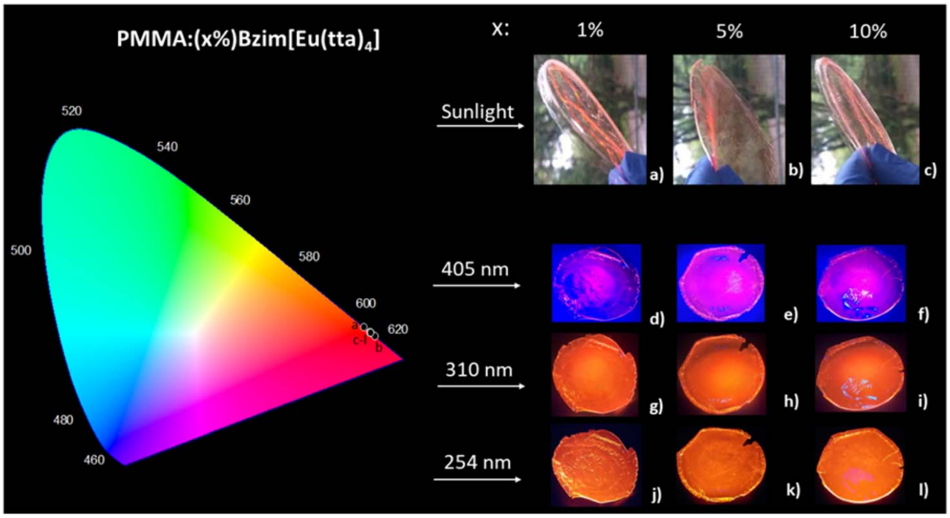

Fig. 8 CIE diagram for the doped PMMA:(*x*%)Bzim[Eu(tta)$_4$] films ($x = 1$, 5 and 10) obtained from their emission spectra at 254, 310, 405 nm, and under sunlight exposure. All spectra were registered at 300 K. The inset photographs of the polymeric films were taken with a digital camera, exhibiting their emission colors under different excitation sources, *i.e.*, exposed to sunlight irradiation at an open external environment (a–c), and at 405 (d–f), 310 (g–i) and 254 nm (j–l).

A_{rad} values for the PMMA:(x%)Bzim[Eu(tta)$_4$] (x = 1.5 and 10%) doped films are higher than that for the complex, owing to the increase in the emission intensity. Meanwhile, the A_{nrad} for the PMMA:(5%)Bzim[Eu(tta)$_4$] and PMMA:(10%)Bzim[Eu(tta)$_4$] are lower than that for the corresponding complex, suggesting that the Eu^{3+} ion is placed in a more rigid chemical environment. It is interesting to observe the almost negligible influence of the N–H high energy oscillators from the Bzim$^+$ counterion over the Eu^{3+} coordination sphere. Furthermore, the A_{total} value for the complex is lower than that for the doped materials, and the 5 and 10% doped films showed the lowest values. Likewise, the $^5D_0$ emission decay time is lower for the doped films than for the Bzim[Eu(tta)$_4$]·H$_2$O complex, and the PMMA:(5%)Bzim[Eu(tta)$_4$] and PMMA:(10%)Bzim[Eu(tta)$_4$] materials revealed the most promising results (Table 1). Finally, the intrinsic quantum yield ($Q^{\mathrm{Eu}}_{\mathrm{Eu}}$) for the complex was found as 45%. Meanwhile, for the doped films, the $Q^{\mathrm{Eu}}_{\mathrm{Eu}}$ values are higher than those for the complex, but there are similarities between them with an average value of 59%.

Based on the spectroscopic data of the Bzim[Eu(tta)$_4$]·H$_2$O complex, an energy level diagram (Fig. 7) was built to elucidate their intramolecular energy transfer pathways. In the first step, the incoming radiation is absorbed by the tta ligand, which is then excited from a fundamental singlet (S$_0$) to a first excited (S$_1$) state. Subsequently, the energy is nonradiatively transferred through an intersystem crossing (ISC) to an excited triplet (T$_1$) level. Finally, a T$_1$ → Eu^{3+} energy transfer takes place *via* either the $^5D_1$ or $^5D_0$ states, the latter decaying radiatively to its $^7F_{6-0}$ ground levels. The partial energy level diagram (Fig. 7) indicates that the high luminescence intensity of the solid-state Eu^{3+}-complex can be rationalized by the suitable energy gap between the ligand-centered T$_1$ state (based on the zero-phonon transition of the phosphorescence band, Fig. 4) and the main excited energy level of the Eu^{3+} ion ($^5D_1$ and $^5D_0$ with $\Delta E \sim 1860$ and 3600 cm^{-1}, respectively). In addition, it is possible to assign the participation of the Bzim$^+$ counterion in the energy transfer process at some degree, given the chemical interactions such as hydrogen bonding between the cation and one of the carbonyl oxygens from the tta moiety, which can lead to an influence upon the charge density around the Eu^{3+} ion.[31]

The coordinates in the CIE (Commission Internationale l'Eclairage) chromaticity diagrams (Fig. 8) were determined based on the emission spectra of the Eu^{3+}-complex and the doped PMMA:(x%)Bzim[Eu(tta)$_4$] films under excitation at 254 (UVC), 310 (UVB), 405 (UVA) nm and sunlight exposure. All points are quite close to the edge of the diagram, indicating the highly monochromatic character of the doped materials, and the corresponding x, y coordinates showed similar values (Table S2†).

Conclusion

New tetrakis Bzim[Ln(tta)$_4$]·H$_2$O complexes (Ln^{3+} = Eu and Gd) were synthesized, and the Eu^{3+}-complex was successfully doped into a PMMA polymer matrix at 1, 5, and 10% mass concentration. The thermal stability of the complex and the doped material is relatively high and with similar values. Raman spectroscopy indicated the influence of the tetrakis complex upon the microenvironment of the PMMA matrix and a joint chemical interaction between them. An X-ray crystallographic study of the Bzim[Eu(tta)$_4$]·EtOH has shown that this complex is stabilized by several intermolecular interactions, such as N–H⋯O hydrogen bonding, C–H⋯F, and O–H⋯O and halogen bonding interactions, which consolidate and strengthen the formation of this molecular system.

The Gd^{3+}-complex phosphorescence data reveal that the T$_1$ state of the ligand is located at around 20 830 cm^{-1} and thus, in a suitable position for an efficient energy transfer process. Thus, the Bzim[Eu(tta)$_4$]·H$_2$O complex showed high-intensity red emission when excited at the UVC (254 nm), UVB (310 nm), and UVA (405 nm) regions, arising mainly from the $^5D_0 \rightarrow {}^7F_2$ transition (612 nm). The emission spectra of the PMMA:(x%) Bzim[Eu(tta)$_4$] films also revealed strong red emission when exposed to sunlight irradiation in an open external environment. In addition, their CIE diagram points to a highly monochromatic emission irrespective of the excitation wavelength, and the CIE diagram coordinates are all located at the edge of the diagram, indicating a highly monochromatic emission character. The complexes showed a high emission quantum yield in their crystalline powder form, which is explained by the fact that the solvent molecules are not directly coordinated with the metal ion. Furthermore, the experimental intensity parameters show the powerful probing properties of the europium(III) ion even outside the first coordination sphere. Thus, these versatile luminescent-doped materials can find applications as light-converting molecular devices.

Data availability

The data supporting this article have been included as part of the ESI.† Crystallographic data for Bzim[Eu(tta)$_4$]·EtOH have been deposited at the CCDC under 2380427 Identifier. These data can be obtained from the Cambridge Crystallographic Date Center *via* **https://www.ccdc.cam.ac.uk/structures/**

Author contributions

I. P. Assunção: conceptualization, methodology, investigation, data curation, writing – original draft, writing – review & editing, visualization. I. F. Costa: investigation, data curation, writing – original draft, writing – review & editing, visualization. L. Blois: investigation, data curation, writing – original draft, writing – review & editing, visualization. M. C. F. C. Felinto: writing – review & editing, funding acquisition. V. M. Deflon: investigation, data curation, writing – original draft, writing – review & editing, visualization. R. A. Ando: investigation, writing – original draft, writing – review & editing, visualization. O. L. Malta: writing – original draft, writing – review & editing, visualization. H. F. Brito: writing – review & editing, supervision, funding acquisition.

Conflicts of interest

There are no conflicts to declare.

Acknowledgements

The authors are grateful to the Brazilian funding agencies CNPq and FAPESP for financial support. This work was developed within the scope of the Thematic Project FAPESP (Grant 2021/08111-2) "Development of Rare Earth based light converters: Luminescent Markers, Optical Sensors and Amplifiers". Rômulo A. Ando is thankful for the funding (Grant 2022/11983-4). L. Blois is thankful to FAPESP for the PhD scholarship (Grant 2020/16795-6). I. F. Costa is grateful to FAPESP for the post-doc fellowship (Grant 2022/12709-3). Hermi F. Brito and Rômulo A. Ando are grateful to CNPq for the research grants (308872/2022-3 and 306885/2021-2). I. P. Assunção is thankful to the Federal Institute of Education, Science and Technology of São Paulo.

References

1 International Monetary Fund, *Surging Energy Prices in Europe in the Aftermath of the War: How to Support the Vulnerable and Speed up the Transition Away from Fossil Fuels*, IMF Working Papers, 2022.
2 T. Kåberger, *Glob. Energy Interconnect.*, 2018, **1**, 48–52.
3 W. F. Lamb, T. Wiedmann, J. Pongratz, R. Andrew, M. Crippa, J. G. J. Olivier, D. Wiedenhofer, G. Mattioli, A. Al Khourdajie, J. House, S. Pachauri, M. Figueroa, Y. Saheb, R. Slade, K. Hubacek, L. Sun, S. K. Ribeiro, S. Khennas, S. De La Rue Du Can, L. Chapungu, S. J. Davis, I. Bashmakov, H. Dai, S. Dhakal, X. Tan, Y. Geng, B. Gu and J. Minx, *Environ. Res. Lett.*, 2022, **16**, 073005.
4 D. Gielen, F. Boshell, D. Saygin, M. D. Bazilian, N. Wagner and R. Gorini, *Energy Strateg. Rev.*, 2019, **24**, 38–50.
5 F. Meinardi, F. Bruni and S. Brovelli, *Nat. Rev. Mater.*, 2017, **2**, 1–9.
6 M. Vasiliev, K. Alameh and M. Nur-E-Alam, *Appl. Sci.*, 2018, **8**, 1–15.
7 M. Kanellis, M. M. de Jong, L. Slooff and M. G. Debije, *Renewable Energy*, 2017, **103**, 647–652.
8 M. G. Debije and P. P. C. Verbunt, *Adv. Energy Mater.*, 2012, **2**, 12–35.
9 J. C. Goldschmidt, W. G. J. H. M. van Sark and T. M. Letcher, in *Luminescent Solar Concentrator., Comprehensive Renewable Energy,* ed. T. Letcher, Elsevier, 2022, pp. 561–581.
10 T. Warner, K. P. Ghiggino and G. Rosengarten, *Sol. Energy*, 2022, **246**, 119–140.
11 A. R. Frias, M. A. Cardoso, A. R. N. Bastos, S. F. H. Correia, P. S. André, L. D. Carlos, V. de Z. Bermudez and R. A. S. Ferreira, *Energies*, 2019, **12**, 451.
12 X. Wang, T. Wang, X. Tian, L. Wang, W. Wu, Y. Luo and Q. Zhang, *Sol. Energy*, 2011, **85**, 2179–2184.
13 S. V. Eliseeva and J.-C. G. Bünzli, *Chem. Soc. Rev.*, 2010, **39**, 189–227.
14 B. K. Gupta, D. Haranath, S. Saini, V. N. Singh and V. Shanker, *Nanotechnology*, 2010, **21**, 055607.
15 J. C. G. Bünzli, *J. Lumin.*, 2016, **170**, 866–878.
16 R. Ilmi and K. Iftikhar, *J. Photochem. Photobiol., A*, 2017, **333**, 142–155.
17 L. B. Guimarães, A. M. P. Botas, M. C. F. C. Felinto, R. A. S. Ferreira, L. D. Carlos, O. L. Malta and H. F. Brito, *Mater. Adv.*, 2020, **1**, 1988–1995.
18 O. A. Savchuk, J. J. Carvajal, C. D. S. Brites, L. D. Carlos, M. Aguilo and F. Diaz, *Nanoscale*, 2018, **10**, 6602–6610.
19 L. H. C. Francisco, M. C. F. C. Felinto, H. F. Brito, E. E. S. Teotonio and O. L. Malta, *J. Mater. Sci. Mater. Electron.*, 2019, **30**, 16922–16931.
20 M. Gil-Kowalczyk, R. Łyszczek, A. Jusza and R. Piramidowicz, *Materials*, 2021, **14**, 3156.

21 R. A. S. Ferreira, S. F. H. Correia, A. Monguzzi, X. Liu and F. Meinardi, *Mater. Today*, 2020, **33**, 105–121.

22 I. P. Assunção, I. F. Costa, P. R. S. Santos, E. E. S. Teotonio, M. C. F. C. Felinto, U. Kynast, W. M. Faustino, O. Malta and H. F. Brito, *ACS Appl. Opt. Mater.*, 2023, **1**, 354–366.

23 K. Binnemans, *Coord. Chem. Rev.*, 2015, **295**, 1–45.

24 G. F. de Sá, O. L. Malta, C. de Mello Donegá, A. M. Simas, R. L. Longo, P. A. Santa-Cruz and E. F. da Silva Jr, *Coord. Chem. Rev.*, 2000, **196**, 165–195.

25 O. L. Malta, *J. Lumin.*, 1997, **71**, 229–236.

26 G. E. Buono-core, H. Li and B. Marciniak, *Coord. Chem. Rev.*, 1990, **99**, 55–87.

27 S. I. Weissman, *J. Chem. Phys.*, 1942, **10**, 214–217.

28 W. M. Faustino, O. L. Malta and G. F. de Sá, *J. Chem. Phys.*, 2005, **122**, 054109.

29 J. J. Crosby, G. A. Whan and R. E. Freeman, *J. Phys. Chem.*, 1962, **66**, 2493–2499.

30 R. E. Whan and G. A. Crosby, *J. Mol. Spectrosc.*, 1962, **8**, 315–327.

31 I. F. Costa, L. Blois, T. B. Paolini, I. P. Assunção, M. C. F. C. Felinto, R. T. Moura Jr, R. L. Longo, W. M. Faustino, L. D. Carlos, A. N. Carneiro Neto and H. F. Brito, *Coord. Chem. Rev.*, 2024, **502**, 215590.

32 J. Kai, M. C. F. C. Felinto, L. A. O. Nunes, O. L. Malta and H. F. Brito, *J. Mater. Chem.*, 2011, **21**, 3796.

33 J. C. G. Bünzli, *Coord. Chem. Rev.*, 2015, **293–294**, 19–47.

34 E. Regalado-Pérez, N. R. Mathews and X. Mathew, *Sol. Energy*, 2020, **199**, 82–91.

35 I. Motta, G. Bottaro, M. Rando, M. Rancan, R. Seraglia and L. Armelao, *J. Mater. Chem. A*, 2024, **12**, 22516.

36 Y. Wang, G. Xie, J. Chen, X. Zhang, C. Chen, J. Yin and H. Li, *J. Mater. Chem. C*, 2022, **10**, 11924.

37 P. K. Shahi, A. K. Singh, S. K. Singh, S. B. Rai and B. Ullrich, *ACS Appl. Mater. Interfaces*, 2015, **7**, 18231–18239.

38 A. C. F. Beltrame, A. G. Bispo-Jr, F. S. M. Canisares, R. V Fernandes, E. Laureto, S. A. M. Lima and A. M. Pires, *Soft Matter*, 2023, **19**, 3992.

39 H. F. Brito, O. L. Malta, C. A. Alves de Carvalho, J. F. S. Menezes, L. R. Souza and R. Ferraz, *J. Alloys Compd.*, 1998, **275–277**, 254–257.

40 G. M. Sheldrick, *Acta Cryst.*, 2008, **A64**, 112–122.

41 G. M. Sheldrick, *Acta Cryst.*, 2014, **C71**, 3–8.

42 L. Blois, I. F. Costa, J. Honorato, A. V. Sanches de Araújo, R. A. Ando, A. N. Carneiro Neto, M. Suta, O. L. Malta and H. F. Brito, *Inorg. Chem.*, 2024, **63**, 16861–16871.

43 M. Llunell, D. Casanova, J. Cirera, P. Alemany and S. Alvarez, *SHAPE. Program for the Stereochemical Analysis of Molecular Fragments by Means of Continuous Shape Measures and Associated Tools*, Universitat de Barcelona, Barcelona, 2013.

44 A. Das, S. A. Hussain, H. Banik, D. Maiti, T. Aktar, B. Paul, P. Debnath, L. Sieron, A. Bhattacharya, K. L. Bhowmik, W. Maniukiewicz and P. Debnath, *Polyhedron*, 2024, **247**, 116747.

45 S. T. Hulushe, M. H. Manyeruke, M. Louzada, S. Rigin, E. C. Hosten and G. M. Watkins, *RSC Adv.*, 2020, **10**, 16861–16874.

46 A. R. Nekoei, S. F. Tayyari, M. Vakili, S. Holakoei, A. H. Hamidian and R. E. Sammelson, *J. Mol. Struct.*, 2009, **932**, 112–122.

47 K. Nakamoto, *Infrared and Raman Spectra of Inorganic and Coordination Compounds*, John Wiley & Sons, Inc., Hoboken, NJ, USA, 2008.

48 N. V. Pashchevskaya, M. A. Nazarenko, S. N. Bolotin, A. I. Oflidi and V. T. Panyushkin, *Russ. J. Inorg. Chem.*, 2010, **55**, 1425–1432.

49 S. Mohan, N. Sundaraganesan and J. Mink, *Specrrochimica Acta*, 1991, **47**, 1111–1115.

50 T. M. George, M. J. Sajan, N. Gopakumar and M. L. P. Reddy, *J. Photochem. Photobiol., A*, 2016, **317**, 88–99.

51 H. Liang, Z. Zheng, Z. Li, J. Xu B. Chen, H. Zhao, Q. Zhang and H. Ming, *Opt. Quant. Electron*, 2004, **36**, 1313–1322.

52 R. D. Shannon and C. T. Prewitt, *Acta Crystallogr. Sect. B Struct. Crystallogr. Cryst. Chem.*, 1969, **25**, 925–946.

53 R. D. Shannon, *Acta Crystallogr., Sect. A*, 1976, **32**, 751–767.

54 W. T. Carnall, G. L. Goodman, K. Rajnak and R. S. Rana, *J. Chem. Phys.*, 1989, **90**, 3443–3457.

55 A. N. Carneiro Neto, E. E. S. Teotonio, G. F. de Sá, H. F. Brito, J. Legendziewicz, L. D. Carlos, M. C. F. C. Felinto, P. Gawryszewska, R. T. Moura, R. L. Longo, W. M. Faustino and O. L. Malta, *Handb. Phys. Chem. Rare Earths*, 2019, **56**, 55–162.

56 W. T. Carnall, H. Crosswhite and H. M. Crosswhite, *Energy Level Structure and Transition Probabilities in the Spectra of the Trivalent Lanthanides in LaF$_3$*, Argonne, IL (United States), 1978.

57 G. B. V. Lima, J. C. Bueno, A. F. da Silva, A. N. Carneiro Neto, R. T. Moura, E. E. S. Teotonio, O. L. Malta and W. M. Faustino, *J. Lumin.*, 2020, **219**, 116884.

58 R. T. Moura, A. N. Carneiro Neto, R. L. Longo and O. L. Malta, *J. Lumin.*, 2016, **170**, 420–430.

59 A. Shyichuk, R. T. Moura, A. N. C. Neto, M. Runowski, M. S. Zarad, A. Szczeszak, S. Lis and O. L. Malta, *J. Phys. Chem. C*, 2016, **120**, 28497–28508.

60 H. F. Brito, O. M. L. Malta, M. C. F. C. Felinto and E. E. S. Teotônio, *Luminescence Phenomena Involving Metal Enolates*, John Wiley & Sons, Ltd, 2009, pp. 131–184.

61 G. F. de Sá, O. L. Malta, C. de Mello Donegá, A. M. Simas, R. L. Longo, P. A. Santa-Cruz and E. F. da Silva Jr, *Coord. Chem. Rev.*, 2000, **196**, 165–195.

62 O. L. Malta, H. F. Brito, J. F. S. Menezes, F. R. G. E. Silva, S. Alves, F. S. Farias and A. V. M. de Andrade, *J. Lumin.*, 1997, **75**, 255–268.

63 I. P. Assunção, A. N. Carneiro Neto, R. T. Moura, C. C. S. Pedroso, I. G. N. Silva, M. C. F. C. Felinto, E. E. S. Teotonio, O. L. Malta and H. F. Brito, *ChemPhysChem*, 2019, **20**, 1931–1940.